Detection of flooded urban areas in high resolution Synthetic Aperture Radar images using double scattering

International Journal of Applied Earth Observation and Geoinformation 28 (2014) 150–159

Contents lists available at ScienceDirect

International Journal of Applied Earth Observation and Geoinformation

journal homepage: www.elsevier.com/locate/jag

Detection of flooded urban areas in high resolution Synthetic Aperture Radar images using double scattering☆

D.C. Mason[a,*], L. Giustarini[b], J. Garcia-Pintado[a], H.L. Cloke[c]

[a] Environmental Systems Science Centre, Department of Meteorology, University of Reading, Reading RG6 6AL, UK
[b] Departement Environnement et Agro-Biotechnologies, Centre de Recherche Public - Gabriel Lippmann, 4422 Belvaux, Luxembourg
[c] Department of Geography and Environmental Science, University of Reading, Reading RG6 6AB, UK

ARTICLE INFO

Article history:
Received 12 September 2013
Accepted 3 December 2013

Keywords:
Flood detection
Synthetic Aperture Radar
Urban area
Double scattering

ABSTRACT

Flooding is a particular hazard in urban areas worldwide due to the increased risks to life and property in these regions. Synthetic Aperture Radar (SAR) sensors are often used to image flooding because of their all-weather day–night capability, and now possess sufficient resolution to image urban flooding. The flood extents extracted from the images may be used for flood relief management and improved urban flood inundation modelling.

A difficulty with using SAR for urban flood detection is that, due to its side-looking nature, substantial areas of urban ground surface may not be visible to the SAR due to radar layover and shadow caused by buildings and taller vegetation. This paper investigates whether urban flooding can be detected in layover regions (where flooding may not normally be apparent) using double scattering between the (possibly flooded) ground surface and the walls of adjacent buildings. The method estimates double scattering strengths using a SAR image in conjunction with a high resolution LiDAR (Light Detection and Ranging) height map of the urban area. A SAR simulator is applied to the LiDAR data to generate maps of layover and shadow, and estimate the positions of double scattering curves in the SAR image.

Observations of double scattering strengths were compared to the predictions from an electromagnetic scattering model, for both the case of a single image containing flooding, and a change detection case in which the flooded image was compared to an un-flooded image of the same area acquired with the same radar parameters. The method proved successful in detecting double scattering due to flooding in the single-image case, for which flooded double scattering curves were detected with 100% classification accuracy (albeit using a small sample set) and un-flooded curves with 91% classification accuracy. The same measures of success were achieved using change detection between flooded and un-flooded images. Depending on the particular flooding situation, the method could lead to improved detection of flooding in urban areas.

1. Introduction

Flooding is a major hazard in both rural and urban areas worldwide, but it is in urban areas that the risks to people and the economic impacts are most severe. In the UK, for example, over 2 million properties, the majority of them in urban areas, are located in floodplains. An estimated 200,000 of these properties are classified as at risk because they do not have protection against a 1 in 75 year flood event (Evans et al., 2004). This figure may rise further with climate change, especially as the observed increase in the intensity of heavy rainstorms with temperature rise is larger than that predicted (Allan and Soden, 2008).

Nowadays, imaging of flooding is carried out routinely using both satellite and airborne sensors. Synthetic Aperture Radar (SAR) sensors are preferred for flood detection rather than visible band sensors because of their ability to penetrate the cloud that is often present at times of flood, and to image at night-time as well as during the day. A number of active SARs with spatial resolutions as high as 3 m or better have recently been launched that are capable of detecting urban flooding. They include TerraSAR-X, RADARSAT-2 and the four satellites of the COSMO-SkyMed constellation. The latter is particularly useful because it allows image sequences of urban flooding to be built up with 12- or 24-hour revisit intervals. In the absence of significant wind, rain or turbulent surface currents, flooded urban areas generally appear dark in a SAR image

* Corresponding author. Tel.: +44 118 378 5218; fax: +44 118 378 6413.
E-mail addresses: d.c.mason@reading.ac.uk (D.C. Mason), giustari@lippmann.lu (L. Giustarini), j.garcia-pintado@reading.ac.uk (J. Garcia-Pintado), h.l.cloke@reading.ac.uk (H.L. Cloke).

0303-2434/$ – see front matter © 2013 The Authors. Published by Elsevier B.V. All rights reserved.
http://dx.doi.org/10.1016/j.jag.2013.12.002

due to specular reflection from the water surface. Roads and tarmac areas also exhibit low backscatter, though not as low as undisturbed water.

There are two main reasons why SARs are important for the detection of urban flooding. Firstly, the ability to obtain a synoptic overview of the extent of urban and rural flooding both day and night even if cloud is present could be a useful tool for operational flood relief management. The Pitt Report (2008) set out to consider what lessons could be learned from the UK floods of 2007. Among its many recommendations was the need to have real-time or near real-time flood visualisation tools available to enable emergency responders to react and manage fast-moving events, and to target their limited resources at the highest priority areas. It was felt that a simple GIS that could be updated with timings, water levels and extents of flooding during a flood event would be a useful system to keep the emergency services informed. Mason et al. (2012a) describe a prototype near real-time flood detection algorithm for urban and rural areas using high resolution SAR images. The method assumes that a processed multi-look geo-registered SAR image can be delivered to the user in near real-time. Whilst this is not yet possible for newer high resolution SARs such as TerraSAR-X and COSMO-SkyMed, the technology already exists in ESA's FAIRE system for medium resolution ASAR data (Cossu et al., 2009), and processed SAR images from the future Sentinel-1 mission are planned to be available one hour after image reception at the ground station.

Secondly, SAR data may be used as calibration, validation and assimilation data for urban flood inundation models. Such models are important tools for the prediction of risk from flooding in urban areas. They are hydraulic models that solve the shallow water equations at each node of a regular or irregular grid covering the river channel and floodplain, subject to boundary conditions that include the input flow rate to the domain (e.g. Bates et al., 2006). Flood modelling in urban areas is more complicated than in rural areas, as the interaction of flows with the built environment must be modelled. Surface flows are affected not only by ground topography and vegetation, but also by buildings and other man-made features (walls, roads, kerbs, parked vehicles, etc.) (Hunter et al., 2008). Subsurface flows in storm water drainage systems must also be modelled, and coupled with surface flows. Two-dimensional urban flood models need considerable data for their parameterisation. LiDAR data at sub-metre spatial resolution are used to provide highly resolved Digital Surface Models of the urban environment. The other main parameters are the bottom friction factors for the channel and floodplain, with the floodplain friction differing for different surface types (vegetation, roads, etc.). The calibration approach involves adjusting these parameters to minimise the difference between the SAR-observed and modelled flood extents (e.g. Aronica et al., 2002). In addition, assimilation may be used to correct the model state and improve estimates of the model parameters and external forcing. Distributed water levels may be estimated along the SAR flood extents by intersecting them with the floodplain topography, and the water levels at various points along the modelled reach may be assimilated into the model run (e.g. Giustarini et al., 2011; Garcia-Pintado et al., 2013; Mason et al., 2012b).

A difficulty of urban flood detection using SAR is that, due to its side-looking nature, substantial areas of urban ground surface may not be visible to the SAR due to radar shadowing and layover caused by buildings or taller vegetation. For example, Soergel et al. (2003) found that, in airborne SAR data of Karlsruhe, only one-third of the total road surface was visible to the SAR. This makes SAR less effective at detecting urban flooding than it might otherwise be. Consider the case of a road between two buildings as in Fig. 1, with the SAR azimuth direction normal to the paper. Ground (CD) will be in radar shadow as it is hidden from the radar by an adjacent intervening building. The shadowed area will appear dark, and may be misclassified as water even if it is dry. In contrast, an area of flooded ground (AB) in front of the wall of a building may be allocated to the same range bin as the wall, causing layover which generally results in a strong return, and a possible misclassification of flooded ground as un-flooded. Soergel et al. (2003) showed that an object on the road (Y) will only be sensed properly if a condition for the road width w_s holds:

$$w_s > CD + AB = h_2 \quad \tan\theta + h_1 \quad \cot\theta \tag{1}$$

where θ is viewing angle and h_1 and h_2 are building heights. Assuming $\theta = 20^\circ$ and $h_1 = h_2 = 10$ m, a road narrower than 30 m will thus be totally in shadow/layover.

This loss of visibility in flood detection has been quantified in a study by Mason et al. (2010) that used a TerraSAR-X image containing urban flooding together with contemporaneous aerial photography for validation of the TerraSAR-X result. This employed a SAR simulator in conjunction with a LiDAR Digital Surface Model (DSM) to estimate regions of the image in which water would not be visible due to shadow or layover caused by buildings and taller vegetation. Fig. 2 shows the LiDAR DSM of the Tewkesbury area, while Fig. 3 shows those parts of the image not visible to the SAR due to radar shadow and layover. The study found that 76% of the urban water pixels that were actually visible to TerraSAR-X were correctly detected. However, if all the urban water pixels

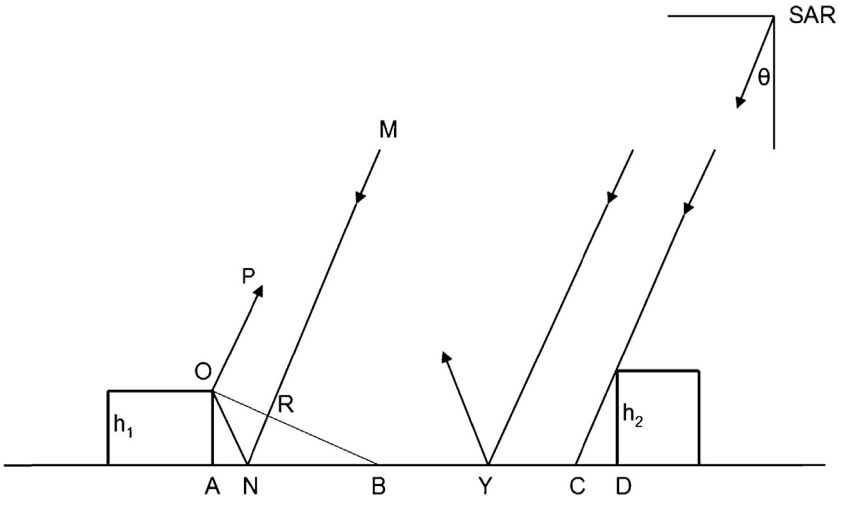

Fig. 1. Layover (AB) and shadow (CD) regions in a flooded street (AD) between adjacent buildings of height h_1 and h_2 (θ = incidence angle).

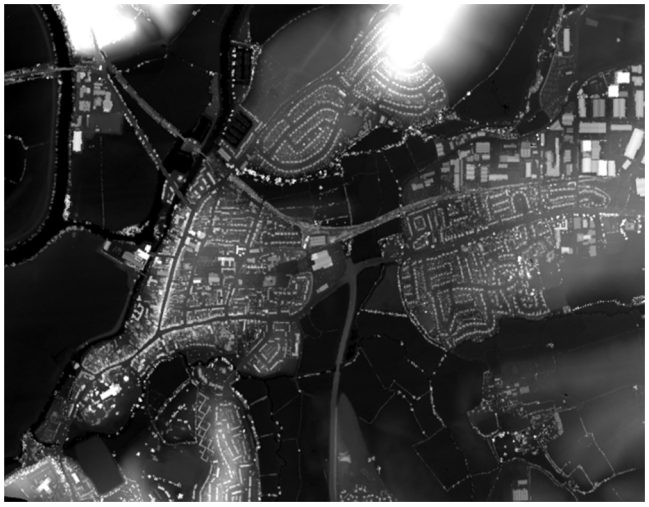

Fig. 2. LiDAR Digital Surface Model of Tewkesbury (lighter = higher) (after Mason et al., 2010).

were considered, including those in shadow and layover areas, this figure fell to 58%. The pattern that emerges is that most flooding along roads perpendicular to the satellite direction of travel can be detected successfully, whereas a good deal of the flooding along roads parallel to the travel direction remains unseen. One strategy that can be used to estimate this unseen flooding is to grow detected urban flood regions where possible by merging them with shadow and layover regions bordering them and of lower or similar ground height. While over a large area of flooding water levels may vary substantially due to the dynamic nature of the flood wave moving down the river, over a small region it is probably fair to assume that water levels will be fairly constant. This approach was used by Mason et al. (2012a), who found that while there was indeed an increase in the urban flood classification accuracy, this was offset by an increase in misclassification as regions incorrectly classified as flooded were also grown.

Another strategy that could be used as a clue to identify unseen urban flooding is to use the double scattering that occurs between roads and adjacent building walls. If the road in a layover region is flooded, backscatter due to the double scattering from sensor to road to wall to sensor (or vice versa) should be stronger than if the road is not flooded (when the road backscatter is from asphalt) (see below). This is illustrated by ray MNOP (or its reverse PONM) in Fig. 1. The double scattering is evident as a bright line or curve at the ground range corresponding to that of the base of the wall (Guida et al., 2010). The effect would be apparent in roads that are roughly parallel to the satellite direction of travel, which is precisely where flooding is largely unseen.

Fig. 4 illustrates how radar returns from different parts of a building and adjacent road are mapped into the slant range of a SAR image due to the fact that they reach the receiver at different times. Proceeding from near to far slant range at constant azimuth, a bright stripe corresponding to the superposition of backscatter from the ground, wall and roof (i.e. to layover) is first found. This is followed by a (usually) brighter return corresponding to wall-ground and ground-wall double scattering. The high intensity of this return is partly due the fact that the double scattering ray paths all have the same length, corresponding to the range of the base of the wall (Guida et al., 2010). Next there may be a dark area corresponding to higher-order multiple (e.g. triple) scattering (usually negligible compared to the other contributions), and finally, a still darker area corresponding to building shadow. When mapped into the 2D ground range-azimuth image, the shape of the double reflection return follows that of the ground-wall intersection, namely a curve which in urban areas is often quasi-linear.

Several authors have shown that the backscatter due to double scattering between a flooded road and wall is substantially greater than that between an asphalt surface and wall (assuming that water depth is small compared to wall height). Watanabe et al. (2010) showed that this was so in HH polarised images, both theoretically and experimentally.

In a further experimental study, Rykhus and Lu (2007) have detected urban flooding in RADARSAT-1 data (after first identifying the urban areas in Landsat ETM+ data) by searching for stronger returns caused by double scattering from flooded streets and adjacent buildings than the returns from adjacent un-flooded urban areas, though the resolution was low (25 m).

Dong et al. (1997) developed a simple model of double scattering from wall-ground structures using a Physical Optics (PO) approximation. The angular variables in their model are the incidence angle θ and the aspect angle φ, where φ is the angle that the intersection line of the wall and road makes with the SAR direction of travel, with

Fig. 3. Regions unseen (black) by TerraSAR-X in LiDAR DSM due to combined shadow and layover (satellite looking West) (after Mason et al., 2010).

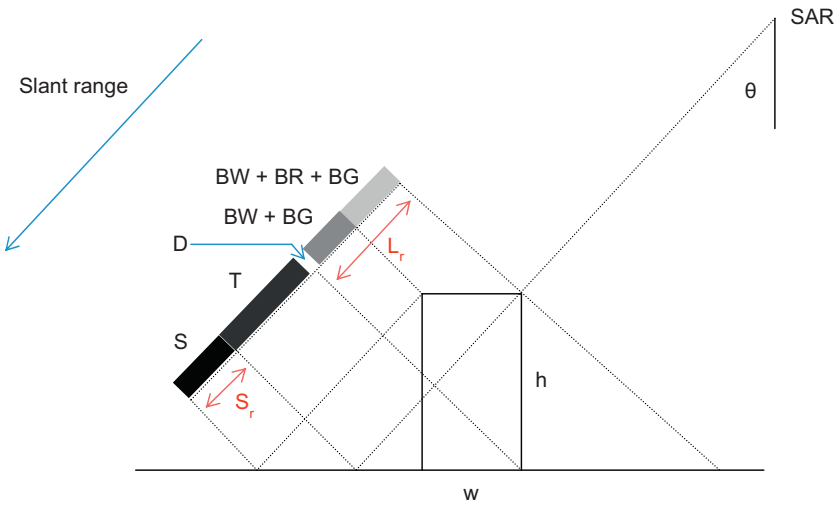

Fig. 4. Composition of different contributions in the SAR slant range (after Guida et al., 2010). BW, backscattering from wall; T, triple scattering; BR, backscattering from roof; L_r, slant range size of layover; BG, backscattering from ground; S_r, slant range size of shadow; D, double scattering; S, shadow; h, building height; w, building width.

$\varphi = 0^\circ$ when this line is parallel to the direction of travel. Using their model, assuming $\theta = 30^\circ$, $\varphi = 0^\circ$ and standard values for the complex dielectric constants of water and asphalt, it can be deduced that the ratio of the backscattering cross-section of wall-water to that of wall-asphalt in HH polarisation is 12 dB. This is primarily because the permittivity of water is higher than that of asphalt. The model also shows that the double scattering cross-section σ_{HH} decreases rapidly as φ is increased (proportional to $\cos^8\varphi$), so that if $\varphi = 30^\circ$, σ_{HH} is only about 30% of that at $\varphi = 0^\circ$.

Iervolino et al. (2011) have used double scattering to develop a method of local flooding level estimation in urban areas using single SAR images. They use the rationale developed by Franceshetti et al. (2002) to associate the building wall height h above the ground surface to the contribution of the double scattering to the radar cross section σ^0:

$$\sigma^0 = h \cdot f(\boldsymbol{p}) \tag{2}$$

where $\boldsymbol{p}$ is a vector of known parameters, $\boldsymbol{p} = (l, \sigma, L, \varepsilon_w, \varepsilon_s, \theta, \varphi)$. Here l is the building length, σ and L are respectively the standard deviation and the correlation length of the stochastic process representing the ground surface, ε_w is the complex dielectric constant of the building wall and ε_s is the complex dielectric constant of the ground surface. The function $f(\boldsymbol{p})$ used in the paper is calculated using the GO–GO method of Franceshetti et al. (2002). The Geometrical Optics (GO) method is used to evaluate the electromagnetic field from the sensor scattered by the ground to the wall (first bounce), and also the field scattered by the wall to the sensor (second bounce) (and vice versa). $f(\boldsymbol{p})$ is given by:

$$f(\boldsymbol{p}) = \frac{\left|S_{qr}\right|^2 l \tan\theta \cos\varphi(1+\tan^2\theta \sin^2\varphi)\exp[-(\tan^2\theta \sin^2\varphi/(2\sigma^2/(2/L^2)))]}{8\pi^2\sigma^2(2/L^2)\cos^2\theta} \tag{3}$$

where S_{qr} is the relevant element of the scattering matrix, with q and r standing for horizontal and vertical polarisation respectively. Expressions for S_{qr} (which depends on ε_w, ε_s, θ and φ) are given in Franceshetti et al. (2002). The GO approach assumes that the ground surface is relatively rough, and can be used provided $k\sigma \gg 1$ (k = radar signal wave number). An alternative approach that might have been used to calculate $f(\boldsymbol{p})$ is the GO–PO method of Franceshetti et al. (2002), where the Physical Optics approximation is used to evaluate the field from the sensor scattered by the ground to the wall (or vice versa). GO–PO is suitable for lower ground roughnesses than GO–GO, but unlike the latter does not have a closed form solution. The grey level intensity of a double scattering return in the SAR image is linked to σ^0 using a calibration technique, whereby one multiplicative constant c and one additive constant d must be included in (2), and height h is the difference between the building wall height h_A and the height of the flood-water h_W, i.e.:

$$\sigma^0_A = c(h_A - h_W) \cdot f(\boldsymbol{p}) + d \tag{4}$$

By employing two reference buildings of different known heights as well as the building of interest, it is possible to write three equations like (4), and so solve for c, d and σ^0_A. In bright areas of SAR images d is often negligible, and, if this is assumed, only one reference building is needed (Guida et al., 2010). The extraction of double scattering curves is performed manually.

Iervolino et al. (2011) try to answer the question "Given that a building is known to be surrounded by flood-water of an unknown depth, and that the height of the building above the un-flooded ground is known, can the change in the double scattering between water and building wall due to the change in effective wall backscattering height be used to estimate the depth of the flood water locally?" This is somewhat different from the question that we want to answer, which is "Is this area of backscatter caused by a double scattering involving water and wall, or asphalt and wall, assuming that the local flood level is approximately known?"

A comparison of the double scattering from the same building in the flooded and un-flooded images is given in Fig. 5. Fig. 5a shows the isolated building in the LiDAR image. Fig. 5b shows the double scattering in the flooded SAR image, given that TerraSAR-X was travelling approximately North to South and looking West. Fig. 5c shows the lower-strength scattering in the un-flooded image.

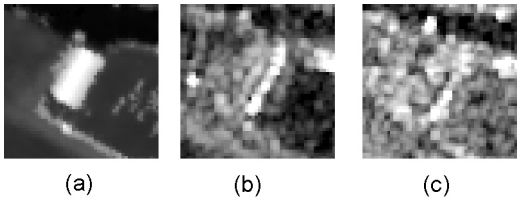

Fig. 5. Example of double scattering from isolated building in flooded and un-flooded SAR images. (a) Isolated building in LiDAR image, and double scattering in (b) flooded image, (c) un-flooded image (satellite looking West).

The regions of flooding detected by their strong double scattering could act as additional clues to the flooding that could be combined with the flood regions detected in urban areas that were not in radar shadow or layover. This would increase the total area of urban water pixels detected by the SAR, and allow the urban flooding that existed to become more visible to the SAR.

The objective of this work is to increase the effectiveness of high resolution SAR at detecting urban flooding by exploiting the increased double scattering that may occur between ground surfaces and building walls when the surface is flooded. Its novelty lies in the fact that it estimates double scattering strengths using a SAR image in conjunction with a high resolution LiDAR height map of the urban area. The LiDAR DSM, in conjunction with a SAR simulator, can be used to estimate areas of radar layover and shadow caused by buildings. It also contains the positions of the intersections of the building walls with the ground surface, which are the positions at which double scattering should occur in the ground range image. In the UK, most major urban areas in flood-plains have now been mapped with airborne LiDAR, and the same is true for urban areas in many other developed countries.

2. Study site and data set

The data set used for this study was acquired for the 1-in-150-year flood that took place on the lower Severn around Tewkesbury, UK, in July 2007 (Mason et al., 2010). This resulted in substantial flooding of urban and rural areas, about 1500 homes in Tewkesbury being flooded. Tewkesbury lies at the confluence of the Severn, flowing in from the northwest, and the Avon, flowing in from the northeast. TerraSAR-X acquired a 3 m-resolution (1.5 m pixel spacing) X-band StripMap image of the region, showing great detail of the flooded urban areas. The TerraSAR-X incidence angle was 24°, and the image was multi-look ground range spatially enhanced. The HH polarisation mode chosen provided good discrimination between flooded and non-flooded regions. At the time of overpass, there was relatively low wind speed and no rain. Contemporaneous aerial photos of the flooding were also acquired, and these were used to validate the flood extent extracted from the TerraSAR-X image. The data set also included LiDAR data (2 m resolution, 0.1 m height accuracy) of the un-flooded area. Further details of this data set are given in Mason et al. (2010).

In addition, a reference TerraSAR-X image of the un-flooded area was acquired almost exactly one year after the flood to allow comparison between flooded and un-flooded areas (Giustarini et al., 2013). This was acquired from the same orbit and with the same incidence angle, polarisation and resolution as the flood image. The vegetation state should also be similar in both images, as they were acquired at the same time of year. Normally, a pre-flood un-flooded image would be used as a comparison, but as TerraSAR-X was still in its commissioning phase in July 2007, a post-flood reference was selected instead. The images were calibrated and geo-referenced, and filtered with a 3×3-pixel Gamma-MAP filter to reduce speckle. The processed flood and reference images are shown in Fig. 6.

This combination of flooded and un-flooded high resolution SAR imagery, together with a LiDAR DSM and aerial photos for validation of flooding, make this data set a valuable resource for the present study. In particular, it is difficult to obtain a data set containing high resolution SAR imagery of a river flood in an urban area as well as contemporaneous aerial photography that can be used to validate the SAR urban flood extent.

3. Detection of double scattering

Two approaches were used to identify double scattering in flooded urban areas. The first used a single SAR image containing flooded areas. Much of the urban area in the TerraSAR-X image is un-flooded, and it is known from the aerial photos which areas are flooded and which are not. In the normal case only a SAR flood image would be available and no aerial photos, but un-flooded urban areas could still be detected in the SAR image by looking for areas above the local flood height. The aim was to see if double scatterings from flooded urban areas were significantly stronger than those from un-flooded ones, given buildings of similar height above surface and aspect angle. It is advantageous to be able to use a single SAR image containing flooding for this because of the difficulty in general of obtaining a pre-flood un-flooded image having the same parameters as the flood image.

The second approach used change detection between the flooded and un-flooded images. The advantage in this case was that the double scattering from an edge of a building surrounded by flood-water in the flooded image could be compared in the two images knowing that the associated un-flooded building heights and aspect angles were the same in both images. The questions asked were, given a set of such flood edges identified in the aerial photo flood map, did these edges give a significantly higher SAR backscatter in the flooded than in the un-flooded image? Did the GO–GO model predict the higher backscatter correctly? Were these the same edges that were classified as flooded using the single flood image? Also, given a set of un-flooded edges from the aerial photos, did these edges give a similar SAR backscatter in the flooded and un-flooded images?

For both approaches, an attempt was made to perform automatic detection of double scattering curves in the SAR image, using the LiDAR DSM of the urban area and its associated radar layover and shadow maps. Strong edges in the DSM (mainly corresponding to building edges) were first detected using a Canny edge detector (Canny, 1986). After an initial smoothing step, this calculates the magnitude and direction of the local gradient at a pixel using a small 3×3-pixel window centred on the pixel, so that curvilinear edges can be detected. The detector subsequently performs non-maxima edge suppression, and applies hysteresis thresholding using an upper and a lower edge threshold, which helps to fill in gaps of lower edge strength pixels between runs of higher edge strength pixels. The regions of layover in the layover map were dilated by 2 pixels to ensure that the ground ranges of these strong edges (mainly corresponding to the bases of walls) were included in the dilated layover areas. Only those edges that occurred in areas of dilated layover and not in areas of shadow were selected. Edges having too large an aspect angle φ to the satellite direction of travel (>40°) were suppressed, as the SAR image is unlikely to exhibit substantial double scattering at these edges. Because in this case aerial photos of the flooding were available, edges in the flooded image known to be in flooded (un-flooded) regions could be selected by suppressing edges outside the flooded (un-flooded) area. Fig. 7 shows the un-flooded edges remaining at this stage. A connected component finder was used to label each remaining edge longer than 2 pixels. At each pixel along the edge its local aspect angle φ determined by the Canny operator was found, and neighbouring pixels in the SAR image along a line centred on the current pixel and perpendicular to φ were examined to find the maximum SAR cross section value within a small distance (± 2 pixels) of the current pixel. The position of this maximum was assumed to be the centre of the double scattering return due to this edge, which should be at the ground range of the base of the wall corresponding to this edge. The maximum values were averaged over the pixels in this edge to estimate the average radar cross section σ^0. This is a spatial multi-look operation in which the averaging process reduces the speckle noise. Also the maximum and minimum heights along this line in the LiDAR DSM were found, corresponding to the local building height and ground height respectively. The maximum heights

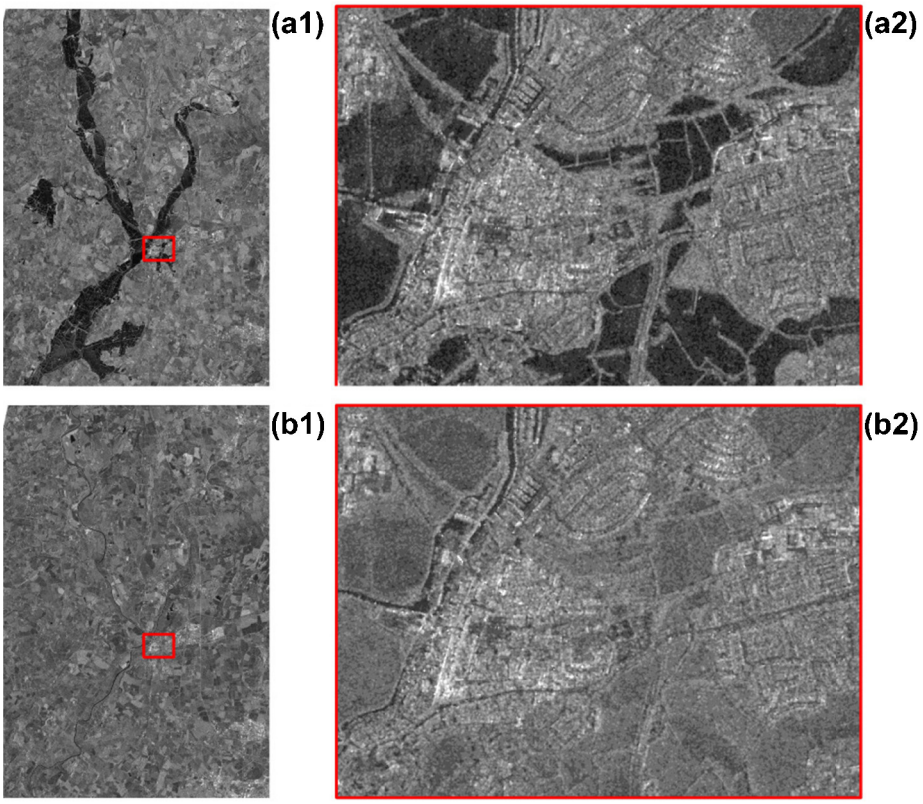

Fig. 6. (a1) Flood image (July 25, 2007) and (b1) reference image (July 22, 2008). The red rectangle shows the zoomed image in the city of Tewkesbury for (a2) the flood image and (b2) the reference (after Giustarini et al., 2013).

at the edge pixels were averaged over the edge pixels to form a mean maximum height for the edge. The same averaging was performed for the set of minimum heights and the set of φ values. In the change detection case, the above processing was applied to both the flooded and un-flooded images.

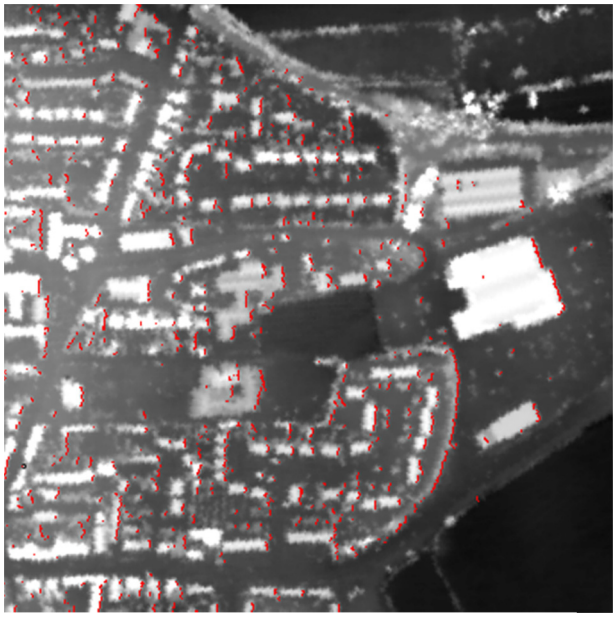

Fig. 7. Un-flooded edges with small aspect angles (red), superimposed upon LiDAR data of central Tewkesbury.

4. Analysis and results

4.1. Single image case

For the single image case, the calibration constant c was determined by selecting a set of edges in un-flooded areas of the flood image that were associated with taller buildings that had small aspect angles. By comparing the observed double scattering with that calculated from Eq. (4) for each edge in the set, an optimum value of c was obtained by adjusting c to minimise the sum of the squared differences (assuming $d = 0$). Note that the normal method of performing radiometric calibration to calculate the radar cross section σ^0 based on the backscatter brightness value from a single target would be inappropriate in this case, as this assumes that a single rather than a double scattering has occurred (Shimada, 2010).

The GO–GO model was used to calculate the double scattering strength in the un-flooded case, given the measured aspect angle φ and building height h_A, and assuming known values for the complex dielectric constants of ground and wall. The values of the parameters used in the model were taken from table III of Guida et al. (2010), and are given in Table 1 (in the former table, the complex dielectric constants for wall and ground are given for a frequency of 1.28 GHz; they were adjusted to X-band frequency in Table 1 using the facts that their permittivities do not change much at these frequencies, while their conductivities can be scaled approximately linearly (Muqaibel et al., 2005)). The value of h_W used in Eq. (4) was the height of the ground adjacent to the edge (h_G).

Fig. 8 shows a regression of observed σ^0 against predicted backscatter factor $(h_A - h_G) \cdot f(\boldsymbol{p})$ for a training set of 9 un-flooded double scattering edges, chosen as a training set to determine the calibration constant. Comparing the observed edges to the model

Table 1
Parameters used in radar backscattering calculations.

Parameter	Value
Complex dielectric constant of wall	$3.0 - j0.07$
Complex dielectric constant of ground	$4.0 - j0.007$
Ground roughness standard deviation (m)	0.19
Ground roughness correlation length (m)	1.54
Complex dielectric constant of water	$55 - j38$
Water roughness standard deviation (m)	0.01
Water roughness correlation length (m)	0.2

predictions is the best way to take variations of building height and aspect angle between edges into account. From the regression line, a calibration constant $c = 77.2 \pm 21.0$ was determined. Using this constant, the difference between the observed and modelled σ^0 for each un-flooded edge was also measured:

$$dRCSg_{1i} = (\text{observed } \sigma^0)_{1i} - (\text{modelled } \sigma^0 \text{ for ground})_{1i} \quad (5)$$

where '1' is the index for the class 'un-flooded' and i is the index for the ith edge. Note that $dRCSg_{1i}$ is positive if the observed σ^0 is larger than or equal to the modelled σ^0.

After determining the calibration constant, the GO–GO model was again used, this time to calculate the double scattering that would be expected if the set of 9 edges was flooded rather than un-flooded. The values of the parameters used for water in the model were taken from table II of Iervolino et al. (2011), and are given in Table 1. Note that the GO approach assumes that the ground surface is relatively rough, and can only be used provided $k\sigma \gg 1$. For the water roughness standard deviation given in Table 1 ($\sigma = 0.01$ m), given $k = 203$/m for X-band SAR (9.65 GHz), $k\sigma = 2$, and this condition is not strictly satisfied. The same complex dielectric constant for wall was used as above. The calculation in Eq. (4) used the estimated height of the flood-water h_W from low un-vegetated slopes in nearby rural areas, as water height could be estimated accurately on these (Mason et al., 2010). Again, the differences between the observed and modelled σ^0 values for these edges (now assumed flooded) were measured ($dRCSw_{1i}$ for the ith edge). A 2D vector $\boldsymbol{dRCS_1} = \{dRCSw_{1i}, dRCSg_{1i}\}$ was constructed from the 1D difference vectors.

A separate training set of 9 edges known from the validation data to be flooded in the image was chosen, and used to ascertain whether their associated double backscatters were consistent with scattering between water and wall, or asphalt and wall. The GO–GO model was again used, firstly to calculate the modelled average brightness assuming the edge was flooded, and the difference $dRCSw_{2i}$ between observed and modelled values; and secondly to calculate the modelled average brightness assuming the edge was un-flooded, and the difference $dRCSg_{2i}$ between observed and modelled values. A second 2D vector $\boldsymbol{dRCS_2} = \{dRCSw_{2i}, dRCSg_{2i}\}$ was constructed from the 1D difference vectors, with the index

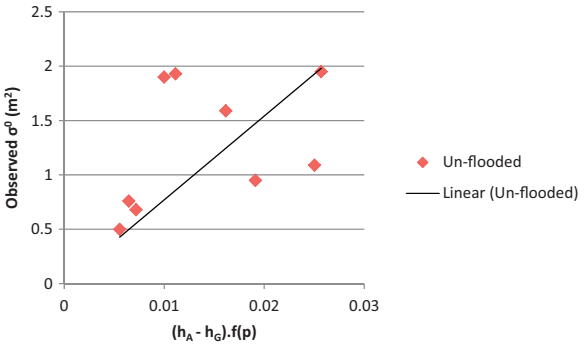

Fig. 8. Regression of observed σ^0 against predicted $(h_A - h_G).f(\boldsymbol{p})$ values for a set of 9 un-flooded double scattering edges.

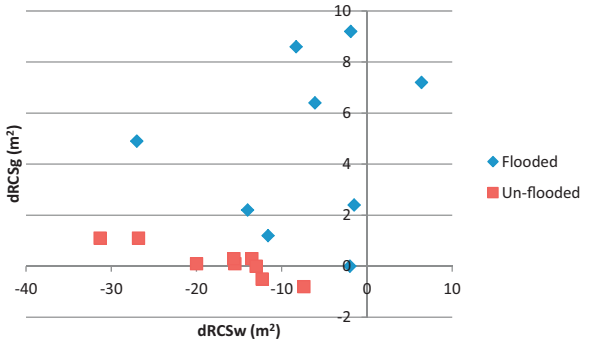

Fig. 9. Plot of $dRCSg$ (observed σ^0-modelled σ^0 for ground) versus $dRCSw$ (observed σ^0-modelled σ^0 for water), for flooded and un-flooded training data sets.

'2' corresponding to the class 'flooded'. Note that these 2D vectors contain errors due to both observations and model predictions.

Fig. 9 shows a plot of $dRCSg$ versus $dRCSw$ for the two training sets of flooded and un-flooded edges. It can be seen that the two classes are reasonably well separated. Table 2 gives the means, standard deviations and correlation coefficients of $dRCSg$ and $dRCSw$ for the two classes. For the un-flooded training set, the mean of $dRCSg_1$ is close to 0 as expected because it is minimised in the regression. However, the mean of $dRCSw_1$ is highly negative, indicating that the modelled brightness assuming that water is the reflector rather than ground is much larger than the observed brightness, giving confidence in the GO–GO model prediction. For the flooded training set, given the standard deviations involved, the mean of $dRCSw_2$ is reasonably close to zero, while the mean of $dRCSg_2$ is positive, indicating that the values predicted by the GO–GO model for flooded rather than un-flooded areas are reasonably in agreement with the observations. This acts as a check that the model with these calibration constants also gives realistic values for edges in the flooded areas, and that the parameter values assumed for water (σ, L, ε_w) given in table II of Iervolino et al. (2011) are reasonable.

Test sets of un-flooded and flooded edges were then examined to see how well these could be classified. For the un-flooded edges, a test set of 22 edges having edge lengths ≥10 pixels and building heights above ground ≥4 m was chosen. Because there was little flooding in the urban area, the training set of flooded edges was also used as the test set. To avoid the classification result for flooded edges being optimistic because the same edge set had been used for test and training data, a leave-one-out strategy was adopted, whereby each flooded edge was classified on the basis of the others in the set. The 2D difference vectors for these sets were subjected to a likelihood ratio test to determine which model would be most likely for each edge. In order to apply the test, the probability distribution for each class was assumed to be 2D normally distributed, with means, standard deviations and correlations given in Table 2. The type of double scattering predicted by the likelihood ratio test was compared to the observed type obtained by knowing whether the edge was in a flooded or un-flooded section of the flood map determined from the aerial photos, and the comparison was used

Table 2
Means, standard deviations and correlations of $dRCSg$ and $dRCSw$ for un-flooded and flooded training data.

State	Variable	Mean (m²)	Stan. dev. (m²)	Correlation coefficient
Un-flooded	$dRCSg_1$	0.2	0.6	−0.92
	$dRCSw_1$	−17.3	7.6	
Flooded	$dRCSg_2$	4.7	3.3	0.18
	$dRCSw_2$	−7.3	9.6	

Table 3
Contingency table for single image case.

	Observed flooded	Observed un-flooded
Predicted flooded	9	2
Predicted un-flooded	0	20

Table 4
Means, standard deviations and correlations of *dRg* and *dRw* for un-flooded and flooded training data.

State	Variable	Mean	Stan. dev.	Correlation coefficient
Un-flooded	dRg_1	−0.07	0.49	−0.32
	dRw_1	−23.7	10.8	
Flooded	dRg_2	3.6	4.0	0.01
	dRw_2	−10.3	15.6	

to update a contingency table (Table 3). This allowed a picture to be built up of how often the predicted type matched the observed type, and how often they differed. It can be seen that all 9 flooded edges, and 20 out of 22 un-flooded edges, were classified correctly.

4.2. Change detection case

An advantage of the change detection case is that it is possible to bypass the calibration step (assuming $d = 0$). The ratio of the calculated double scattering cross-section assuming a water surface (σ^0_w) to that assuming a ground surface (σ^0_g) is given by:

$$\frac{\sigma^0_w}{\sigma^0_g} = \frac{c(h_A - h_W)\cdot f(\boldsymbol{p}_w)}{c(h_A - h_G)\cdot f(\boldsymbol{p}_g)} \quad (6)$$

in which c cancels out, and $\boldsymbol{p}_w(\boldsymbol{p}_g)$ is $\boldsymbol{p}$ for water (ground). The difference between the observed ratio and σ^0_w/σ^0_g, and the difference between the observed ratio and 1.0 (when the edge is un-flooded in both images), can then be subjected to the likelihood ratio test as before. The double scattering strengths calculated by the GO–GO model for the single image case were used again in this case.

For each un-flooded edge in the flooded and un-flooded images, the difference between the observed ratio of backscattering in the flooded to un-flooded images and the modelled ratio assuming that the edge was un-flooded in both images (in which case the ratio is 1) was measured:

$$dRg_{1i} = (\text{observed ratio})_{1i} - 1 \quad (7)$$

where '1' is the index for the class 'un-flooded', and i the index for the ith edge. Also for edge i, the difference dRw_{1i} was measured between the observed ratio and the modelled ratio of flooded edge backscatter to un-flooded edge backscatter. A 2D vector $\boldsymbol{dR_1} = \{dRw_1, dRg_1\}$ was constructed from the 1D difference vectors.

In a similar fashion, for each flooded edge j in the flooded image, the difference dRw_{2j} between the observed ratio of backscattering in the flooded to un-flooded images and the modelled ratio of flooded edge backscatter to un-flooded edge backscatter was measured. Also measured was the difference dRg_{2j} between the observed ratio and the modelled ratio when the edge was un-flooded in both cases (when the ratio is 1). A second 2D vector $\boldsymbol{dR_2} = \{dRw_2, dRg_2\}$ was constructed from the 1D difference vectors, with the index '2' corresponding to the class 'flooded'. Again, note that the 2D vectors contain errors due to both observations and model predictions.

Fig. 10 shows a plot of *dRg* versus *dRw* for the two training sets of flooded and un-flooded edges, for the change detection case. Table 4 gives the means, standard deviations and correlation coefficients of *dRg* and *dRw* for the two classes. The two classes are again

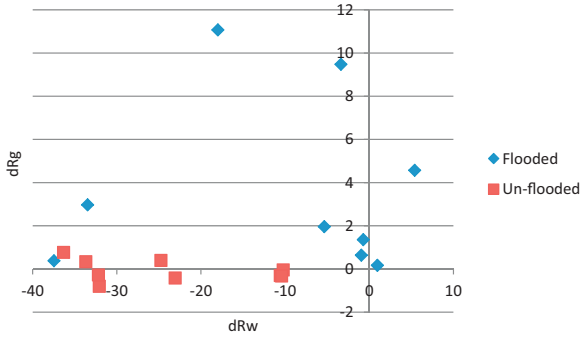

Fig. 10. Plot of dRg (observed ratio-modelled ratio with both edges un-flooded) versus dRw (observed ratio-modelled ratio of flooded to un-flooded edge backscatter), for flooded and un-flooded training data sets.

separated, though not quite as well as in the single image case. This is probably due to additional noise being present in the observed ratio and the modelled ratio of flooded to un-flooded edge backscatter, due to the action of taking ratios. Slight differences in registration between the flooded image and the LiDAR, and the un-flooded image and LiDAR, should be taken into account by the sliding window technique used to find the maximum SAR cross-section value, described in Section 3.

Test sets of un-flooded and flooded edges were examined to see how well these could be classified for the change detection case. For the un-flooded edges, the test set of 22 edges having edge lengths ≥10 pixels and building heights above ground ≥4 m was again chosen. The training set of flooded edges in the flooded image was again used as the test set, and again a leave-one-out classification strategy was employed. The 2D ratio difference vectors for these sets were subjected to a likelihood ratio test to determine which model would be most likely for each edge. In order to apply the test, the probability distribution for each class was assumed to be 2D normally distributed, with means, standard deviations and correlations given in Table 4. The class predicted by the likelihood ratio test was compared to the validation class observed in the aerial photos, and the comparison was used to update a contingency table (Table 5). The results were the same as those for the single image case, with 9 out of 9 flooded edges and 20 out of 22 un-flooded edges being classified correctly. For the flooded edges, the GO–GO model predicted significantly higher backscatter in the flooded than in the un-flooded image, with the mean ratio being 12.8.

4.3. Modification of the flood detection algorithm

The flood detection algorithm of Mason et al. (2010, 2012a) was modified to account for flooding detected via double scattering. For those double scatterings deemed to have arisen from a flooded surface in front of a building, the area of layover in front of the building that was not in shadow and of similar or lower height to the ground adjacent to the building was assumed to be flooded.

A final step was to measure the improvement in the overall urban flood detection accuracy that occurred as a result of the detection of flooding associated with double scattering. Unfortunately, the TerraSAR-X image acquired for the example flood event considered here did not provide a particularly good test of the method. The image was acquired three days after the peak of the

Table 5
Contingency table for change detection case.

	Observed flooded	Observed un-flooded
Predicted flooded	9	2
Predicted un-flooded	0	20

flood when the water had started to subside. Most of the remaining flooding in urban areas lay along three streets roughly perpendicular to the satellite direction of travel, so that they were not very suitable for providing examples of double scattering (see Fig. 13 of Mason et al., 2010). The main street of Tewkesbury, running roughly North-South (parallel to the satellite track) and exhibiting substantial layover (in Fig. 3, the long black street to the left of centre) contained no flooding as it lay above the flood level. Specifically, the fraction of urban water pixels detected as flooded by TerraSAR-X using the modified algorithm (including those pixels lying in shadow or layover areas) increased only slightly from the figure of 58% found by Mason et al. (2010).

Further testing of the method using other images where more flooding occurs along roads parallel to the satellite direction of travel is required. The authors are unaware of any other data set comprising both high resolution SAR images exhibiting significant urban flooding and contemporaneous aerial photography to validate the SAR flood extent, for which LiDAR data can also be obtained. It is a weakness of this paper that the method has not been more thoroughly tested in a more appropriate scenario. The situation is likely to improve in the future as more high resolution SAR images of urban floods are acquired, and further testing of the method is a future goal. However, even though in this particular case the overall flood detection accuracy shows little improvement if flooding detected by double scattering is included, it should be borne in mind that the results of Section 4.2 show that it is possible to distinguish double scattering curves in flooded areas from those in un-flooded areas with good success.

5. Discussion

A full sensitivity analysis of the effects of model structure and parameter error on classification accuracy has not been carried out in this study. As regards model structure error, the classification study could usefully be repeated using the GO–PO rather than the GO–GO model, to examine the effect of using a different scattering model. As regards model parameter error, the errors on parameters h, l and φ used in deriving $f(\boldsymbol{p})$ in Eq. (2) are fairly small due to the accuracy of the LiDAR data. However, the effects of errors in parameters ε_w, ε_s, σ and L are less clear. For example, the single value used for ε_w (the complex dielectric constant of the building wall) assumes that all walls contain the same fractions of brick, glass and other materials, which is too simplistic to cover all cases. This is illustrated by the event in the flooded class at $(dRCSw_2, dRCSg_2) = (6.4, 7.2)$ in Fig. 9. This is produced by the isolated structure of Fig. 5 considered in more detail by Iervolino et al. (2011). These authors show that the structure's wall is largely made of aluminium, so that the predictions of the GO–GO model may be in error in this case. Again, the values used in Table 1 were taken from Guida et al. (2010), who carried out simulations using buildings placed on rough soil, and it is fair to question whether the ground parameters used in their simulations can be taken over to the present case. While some of the edges sampled were adjacent to fields, the majority were adjacent to roads, pavements and house gardens. The model also assumes uniform uninterrupted ground surface adjacent to walls, while in practice some of this surface will generally be occupied by vehicles. However, the difference vectors for the single-image case ($\boldsymbol{dRCS_i}$) and the change detection case ($\boldsymbol{dR_i}$) will contain errors due to both model and observations, for both flooded and un-flooded classes. It has been assumed that the standard deviations of the flooded and un-flooded classes in the difference vector plots are representative of the total errors due to model structure and parameter uncertainties. In spite of these uncertainties, the results indicate that, for both the single image and change detection cases, a good separation between flooded and un-flooded edges can be achieved, due principally to the large difference between the complex dielectric constants of ground and water. For the single image case, Guida et al. (2010) also point out that one effect of the calibration procedure will be to reduce the sensitivity to errors in the parameters.

In the case study considered here, it is known from the aerial photos which areas are flooded and which are not. In the normal case where no aerial photos are available, un-flooded edges could be detected in the flood image by looking in urban areas above the local flood height. In the single image case, the calibration constant c could be determined from these un-flooded edges. For the single image (change detection) case, a 2D normal probability distribution could be constructed from the 2D vector $\boldsymbol{dRCS_1}$ ($\boldsymbol{dR_1}$) of these un-flooded edges. Edges below the flood height could be classified as flooded or un-flooded depending on their match to this distribution.

The results of a double scattering analysis would need to be interpreted with some care to ensure that no other strong reflectors were at the same slant range as the double scattering curve. For example, if there were two similar streets of houses running parallel to the satellite direction of travel, the slant range of the inclined roofs of the houses in the street farther from the satellite track might be the same as that of the double scattering from the house walls in the nearer street. Assuming $\theta = 24^\circ$ and house heights of 10 m, this situation would occur for a street width of about 22 m.

From Eq. (1) and Fig. 1, it is apparent that, at building locations, a small viewing angle leads to large layover areas and small shadow areas, whereas a large viewing angle leads to small layover areas and large shadow areas. The full performance incidence angle range for TerraSAR-X in stripmap mode is 20°–45°. Mason et al. (2010) show that an object on the road will only be sensed properly at $\theta = 20^\circ$ if the road width $w_s > 3.1\,h$, whereas if $\theta = 45^\circ$, $w_s > 2.0\,h$. This implies that the use of larger incidence angles should lead to increased detection of flooded urban pixels. The finding that it is possible to detect flooding in layover areas using the double scattering effect may not detract from this argument. From Fig. 1, the region $AN = h_1 \tan\theta$ is the ground range from which double scattering is generated, whereas ground range $AB = h_1 \cot\theta$ is the layover region. As θ increases from 20°, AN remains less than AB until $\theta = 45^\circ$, when AN = AB. If $\theta = 20^\circ$, increased double scattering may only be detected if the ground immediately adjacent to the building of height h_1 is flooded. On the other hand, if $\theta = 45^\circ$, any flooded areas in the layover region AB may contribute to increased double scattering, though the signal from these may be reduced by lower backscattering from other un-flooded areas in the layover region.

The possibility to use double scattering to help detect urban flooding arises from the fact that conventional SAR sensors are side-looking. The ground range resolution of a SAR sensor is infinite if the incidence angle is zero (i.e. at nadir), and improves as the incidence angle is increased. So a SAR needs to be side-looking to achieve adequate ground range resolution, but unfortunately this can create shadow and layover (Rees, 2001). Altimeters are nadir-looking, but are aimed at measuring surface height from time-of-flight rather than backscatter cross section, and ground range resolution is limited. Even future altimeters such as SWOT, which will use SAR interferometry to measure surface water heights, will have insufficient spatial resolution to resolve most urban features.

The method depends on the availability of a high resolution DSM of the urban area, in this case obtained from airborne LiDAR. LiDAR data have now been acquired for many urban areas in the developed world. One possible future alternative to LiDAR may be very high resolution airborne cross-track SAR interferometry. This should enable the derivation of 3D topographic information of urban areas with good height resolution and spatial resolution in the decimetre range (Schmitt and Stilla, 2011). Again, the side-looking geometry inherent to conventional SAR sensors leads to the production

of radar shadowing and layover. The use of images recorded at different aspect angles has been investigated to fill in the missing information in the shadow area, while research to separate information from different scatterers contained in one layover-affected resolution cell is currently proceeding using multi-baseline data.

6. Conclusion

The study has shown that it is possible to detect flooding in radar layover regions in urban areas using double scattering. The method proved equally successful at detecting this type of flooding in the single-image case and when using change detection between flooded and un-flooded images. Depending on the particular situation (the urban area flooded, the mix of building heights and their orientation to the satellite direction of travel), this may make SAR more effective at detecting urban flooding than if double scattering was ignored. For both the single-image and change detection cases, it proved possible to determine the positions of double scattering curves in the SAR image automatically, using the LiDAR DSM of the urban area and its associated radar layover and shadow maps produced by the SAR simulator. The results show that the GO–GO model performs adequately in predicting flooded and un-flooded double scattering strengths. However, it would be advantageous to compare the GO–GO model predictions with those of the GO–PO model, as part of a full sensitivity analysis of the effects of model structure and parameter error on classification accuracy. Further testing of the method on SAR images of other urban flood events is also required.

Acknowledgements

This work was partly supported by the UK Natural Environment Research Council (NERC) through the DEMON (Developing Enhanced impact Models for integration with Next generation NWP and climate outputs) project, included in the NERC Storm Risk Mitigation programme (NE/I005242/1). Thanks are due to Dr. M. Chini for assistance with processing the images, and to the reviewers for improving the clarity of the paper.

References

Allan, R.P., Soden, B.J., 2008. Atmospheric warming and the amplification of precipitation extremes. Science 321 (5895), 1481–1484.
Aronica, G., Bates, P.D., Horritt, M.S., 2002. Assessing the uncertainty in distributed model predictions using observed binary pattern information within GLUE. Hydrol. Process. 16 (10), 2001–2016.
Bates, P.D., Wilson, M., Horritt, M.S., Mason, D.C., Holden, N., Currie, A., 2006. Reach scale floodplain inundation dynamics observed using airborne SAR imagery. J. Hydrol. 328 (1–2), 306–318.
Canny, J.F., 1986. A computational approach to edge detection. IEEE. Trans. Pattern Anal. Mach. Intell. 8 (6), 679–698.
Cossu, R., Schoepfer, E., Bally, Ph., Fusco, L., 2009. Near real-time SAR based processing to support flood monitoring. J. Real-Time Image Process. 4 (3), 205–218.
Evans, E.P., Ashley, R., Hall, J.W., Penning-Rowsell, E.C., Saul, A., Sayers, P.B., Thorne, C.R., Watkinson, A., 2004. Foresight Flood and Coastal Defence Project: Scientific Summary. Office of Science and Technology, London.
Dong, Y., Forster, B., Ticehurst, C., 1997. Radar backscatter analysis for urban environments. Int. J. Rem. Sens. 18 (6), 1351–1364.
Franceshetti, G., Iodice, A., Riccio, D., 2002. A canonical problem in electromagnetic backscattering from buildings. IEEE Trans. Geosci. Rem. Sens. 40 (8), 1787–1801.
Garcia-Pintado, J., Neal, J.C., Mason, D.C., Dance, S., Bates, P.D., 2013. Scheduling satellite-based SAR acquisition for sequential assimilation of water level observations into flood modelling. J. Hydrol. 495, 252–266.
Giustarini, L., Matgen, P., Hostache, R., Montanari, M., et al., 2011. Assimilating SAR-derived water level data into a hydraulic model: a case study. Hydrol. Earth Syst. Sci. 15 (7), 2349–2365.
Giustarini, L., Hostache, R., Matgen, P., Schumann, G., Bates, P.D., Mason, D.C., 2013. A change detection approach to flood mapping in urban areas using TerraSAR-X. IEEE Trans. Geosci. Rem. Sens. 51 (4), 2417–2430.
Guida, R., Iodice, A., Riccio, D., 2010. Height retrieval of isolated buildings from single high-resolution SAR images. IEEE Trans. Geosci. Rem. Sens. 48 (7), 2967–2979.
Hunter, N.M., Bates, P.D., Neelz, S., Pender, G., Villanueva, I., Wright, N.G., Liang, D., Falconer, R.A., Lin, B., Waller, S., Crossley, A.J., Mason, D.C., 2008. Benchmarking 2D hydraulic models for urban flood simulations. Water Manage. 161 (1), 13–30.
Iervolino, P., Diessa, V., Iodice, A., Ricciardi, A., Riccio, D., Guida, R., 2011. A new local approach for flooding level estimation in urban areas using single SAR images. In: Stilla, U., Gamba, P., Juergens, C., Maklav, D. (Eds.), Joint Urban Remote Sensing Event. April 11–13, Munich, Germany.
Mason, D.C., Davenport, I.J., Neal, J.C., Schumann, G.J.-P., Bates, P.D., 2012a. Near real-time flood detection in urban and rural areas using high resolution Synthetic Aperture Radar images. IEEE. Trans. Geosci. Rem. Sens. 50 (8), 3041–3052.
Mason, D.C., Schumann, G.J.-P., Neal, J.C., Garcia-Pintado, J., Bates, P.D., 2012b. Automatic near real-time selection of flood water levels from high resolution Synthetic Aperture Radar images for assimilation into hydraulic models: a case study. Rem. Sens. Environ. 124, 705–716.
Mason, D.C., Speck, R., Devereux, B., Schumann, G.J.-P., Neal, J.C., Bates, P.D., 2010. Flood detection in urban areas using TerraSAR-X. IEEE. Trans. Geosci. Rem. Sens. 48 (2), 882–894.
Muqaibel, A., Safaai-Jazi, A., Bayram, A., Attiya, A.M., Riad, S.M., 2005. Ultrawideband through-the-wall propagation. IEEE Proc. Microw. Antennas Propag. 152 (6), 581–588.
Pitt, M., 2008. Learning lessons from the 2007 floods. UK Cabinet Office Report, June 2008, Available online at: http://archive.cabinetoffice.gov.uk/pittreview/thepittreview.html
Rees, W.G., 2001. Physical Principles of Remote Sensing, 2nd ed. Cambridge University Press, Cambridge, UK, 343 pp.
Rykhus, R., Lu, Z., 2007. Hurricane Katrina flooding and oil slicks mapped with satellite imagery. In: Farris, G.S., Smith, G.J., Crane, M.P., Demas, C.R., Robbins, L.L., Lavoie, D.L. (Eds.), Science and the Storms: The USGS Response to the Hurricanes of 2005. U.S. Geological Survey Circular 1306. , pp. 49–52.
Schmitt, M., Stilla, U., 2011. Towards airborne single-pass decimeter resolution SAR interferometry over urban areas. Photogrammetric Image Analysis, Lecture Notes on Computer Science, vol. 6952. Springer, Berlin, pp. 197–208.
Shimada, M., 2010. Ortho-rectification and slope correction of SAR data using DEM and its accuracy evaluation. IEEE J. Select. Top. Appl. Earth Observ. Rem. Sens. 3 (4), 657–671.
Soergel, U., Thoennessen, U., Stilla, U., 2003. Visibility analysis of man-made objects in SAR images. In: 2nd GRSS/ISPRS Joint Workshop on Data Fusion and Remote Sensing over Urban Areas, 22–23 May, Berlin.
Watanabe, M., Matsumoto, M., Shimada, M., Asaka, T., Nishikawa, H., Sato, M., 2010. Simultaneous observation data of GB-SAR/PiSAR to detect flooding in urban areas. EUROSIP J. Adv. Sig. Process. 2010, 6 pp., article ID 560512.